

See discussions, stats, and author profiles for this publication at: <https://www.researchgate.net/publication/272663704>

Growth of nano-textured graphene coatings across highly porous stainless steel supports towards corrosion resistant coatings

Article in *Carbon* · February 2015

DOI: 10.1016/j.carbon.2015.02.042

CITATIONS

15

READS

908

14 authors, including:



Dumée Ludovic

Deakin University

81 PUBLICATIONS 1,046 CITATIONS

SEE PROFILE



Mary She

Deakin University

50 PUBLICATIONS 571 CITATIONS

SEE PROFILE



Steve Gray

Victoria University Melbourne

152 PUBLICATIONS 2,806 CITATIONS

SEE PROFILE



Lingxue Kong

Deakin University

317 PUBLICATIONS 2,843 CITATIONS

SEE PROFILE

Some of the authors of this publication are also working on these related projects:



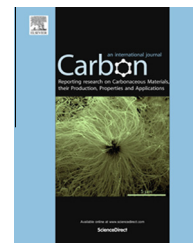
Scalable fabrication of bio-inspired, 3D micro/nanochannel networks [View project](#)



Nanomaterials for Sensing in Body Area Networks [View project](#)

Available at www.sciencedirect.com

ScienceDirect

journal homepage: www.elsevier.com/locate/carbon

Growth of nano-textured graphene coatings across highly porous stainless steel supports towards corrosion resistant coatings

Ludovic F. Dumée ^{a,b,*}, Li He ^a, Ziyu Wang ^{a,c}, Phillip Sheath ^c, Jianyu Xiong ^a, Chunfang Feng ^a, Mike Yongjun Tan ^a, Fenghua She ^a, Mikel Duke ^b, Stephen Gray ^b, Alfredo Pacheco ^d, Peter Hodgson ^a, Mainak Majumder ^c, Lingxue Kong ^a

^a Institute for Frontier Materials, Deakin University, Pigdons Road, 3216 Waurn Ponds, Victoria, Australia

^b Institute for Sustainability and innovation, Victoria University, Hoppers Lane, 3030 Werribee, Victoria, Australia

^c Nanoscale Science and Engineering Laboratory (NSEL), Department of Mechanical and Aerospace Engineering, Monash University, 3800 Clayton, Victoria, Australia

^d Energy and Environment Division, TECNALIA, Paseo Mikeletegi, 20009 San Sebastián, Guipúzcoa, Spain

ARTICLE INFO

Article history:

Received 17 December 2014

Accepted 9 February 2015

Available online 24 February 2015

ABSTRACT

In this paper, we demonstrated for the first time the growth of 3D networks of graphene nano-flakes across porous stainless steel substrates of micron sized metal fibres, and its anti-corrosion properties. The controlled formation of graphene-grade coatings in the form of single sheets to complex and homogeneously distributed 2–4 μm long nano-pillars is demonstrated by Scanning Electron Microscopy. The morphology and stability of these structures are shown to be particularly related to the temperature and feed gas flow rate during the growth. The number of layers across the graphene materials was calculated from the Raman spectra and is shown to range between 3 and more than 15 depending on the growth conditions and to be particularly related to the time and flow rate of the experiment. The presence of the graphene was shown to massively enhance the specific surface area of the material and to contribute to the increased corrosion resistance and electrical conductivity of the material without compromising the properties or structure of the native stainless steel materials. This new approach opens up a new route to the facile fabrication of advanced surface coatings with potential applications in developing new thermal exchangers, separation and bio-compatible materials.

© 2015 Elsevier Ltd. All rights reserved.

1. Introduction

Metal based materials are particularly prone to surface oxidation and corrosion which leads to premature degradation of

metal structures and loss of mechanical strength. Developing more environmentally friendly and cheaper corrosion resistant materials [1–3] will provide alternatives to current anti-corrosion technologies, including toxic hexavalent chromium

* Corresponding author at: Institute for Frontier Materials, Deakin University, Pigdons Road, 3216 Waurn Ponds, Victoria, Australia. Fax: +61 352271102.

E-mail address: ludovic.dumee@deakin.edu.au (L.F. Dumée).

<http://dx.doi.org/10.1016/j.carbon.2015.02.042>

0008-6223/© 2015 Elsevier Ltd. All rights reserved.

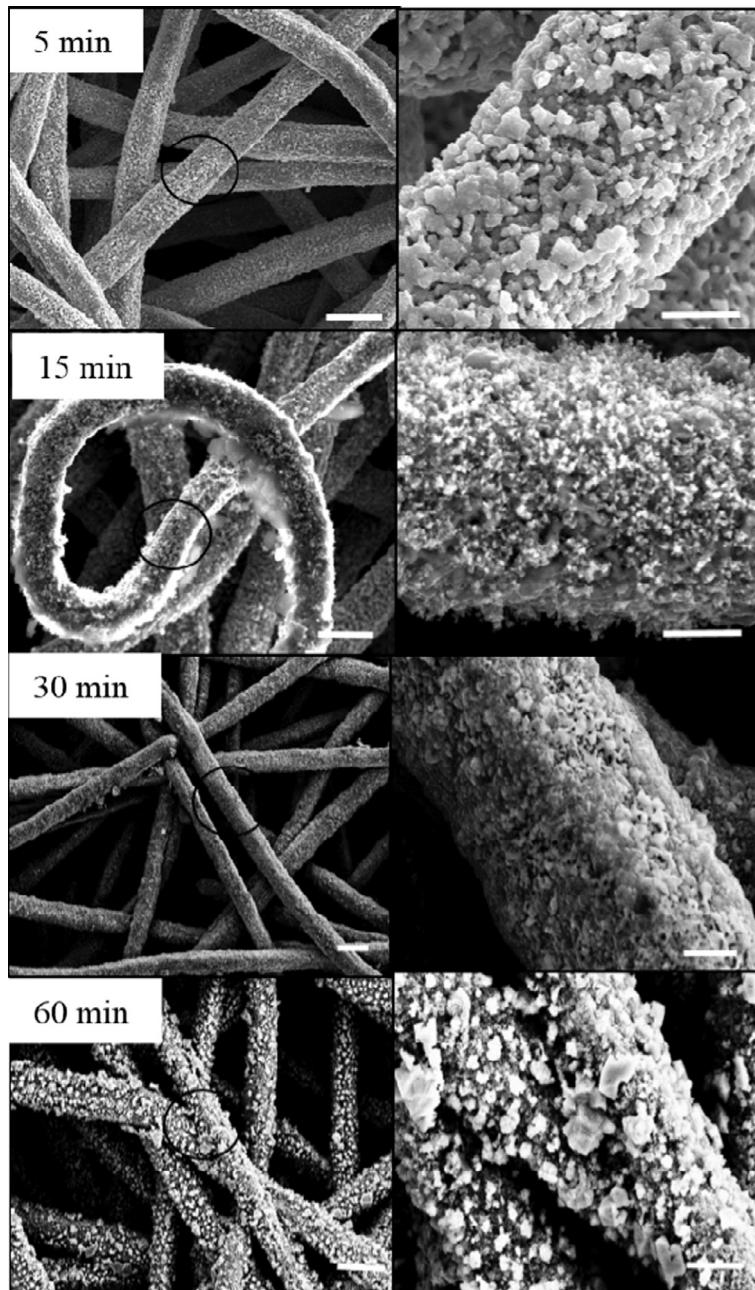


Fig. 1 – Representative SEMs of the hybrid stainless steel graphene samples as a function of the growth time (900 °C and 20 ccm hexane flow rate). The area highlighted with a black circle on the left column of images corresponds to the higher magnification on the right hand side column. Scale bars are 50 μm and 5 μm respectively.

coatings or electroplating which typically have large environmental and process footprints and lead to the generation of large volumes of toxic liquid waste [4,5]. A strategy of developing new protective coatings is the incorporation of new materials that are able to atomically bind with metals and which can improve the behaviour of the interfaces with the surrounding media or the surface properties without compromising the metal thermal or electromechanical properties [6–8].

Graphene offers highly promising opportunities for the development of active platforms with potential applications

in nano-electronics, molecular separation, high strength composites, and the surface coating industries [9,10]. Recently, graphene oxide (GO) and graphene, either deposited or directly grown onto pre-formed surfaces have been shown to prevent electrochemical corrosion by acting as highly efficient impermeable barriers to corrosive species [11,12]. Corrosion is a complex phenomenon that is affected by environmental factors and metal surface conditions such as surface roughness, exposed surface area, surface energy, and the stability of oxides which is intrinsically related to the target material including its composition, purity,

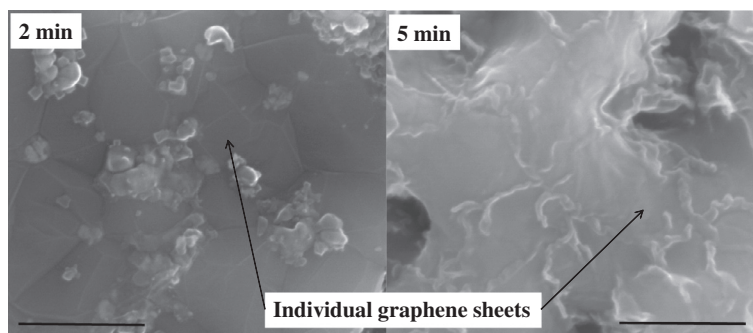


Fig. 2 – Representative high magnification SEMs of the formation of individual graphene sheets on the surface of the stainless steel. Reference SEMs of the stainless steel fibres heat treated in the same conditions but without hexane are also provided (Fig. S2). Scale bars are 500 nm.

crystalline structure, surface energy and roughness. The natural hydrophobicity and conductive properties of the graphene prevent corrosion by simultaneously repelling water and evenly distributing the electric potential across the surface with possible redox reactions that are typically corroding pure metals into metal oxides [13].

Porous metal structures, used as filtration membranes, heat dissipation systems, biomedical scaffolds or sensors are particularly sensitive to corrosion due to their higher surface to volume ratio [2]. However, despite obvious economic incentives, knowledge of atomic-scale processes behind surface metal oxidation and routes to reduce oxidation rates remains rather limited. Strategies to slow down degradation by introducing nano-sized metal oxide layers on the metal surface with a thickness ranging between 2 and 3 nm have been shown to act as a passivation film enabling better corrosion protection [6,8]. Although the presence of nano-sized layers of graphene on the surface of dense and polished metal substrates was demonstrated to enhance the metal corrosion resistance by up two orders of magnitude without otherwise altering the materials thermo-mechanical or electrical properties [12,13], the formation of graphene across rough and porous metal alloy materials, such as stainless steel, is yet to be fully demonstrated. However, the design of novel deposition techniques to form high grade and continuous porous graphene materials is essential which would also benefit areas such sensing, heat-exchange, energy storage and separation [14–16].

In this paper, we demonstrate for the first time the growth of 3D architectures of graphene nano-flakes across porous stainless steel substrates. Austenitic stainless steel fibres (SS316) were used as platforms to grow graphene sheets and nano-pillars. The stability and response of the metal to the growth conditions were investigated. SS316 alloys are typically composed of 2 wt% molybdenum, 16 wt% of chromium and 10 wt% of nickel with the balance iron, with the alloying elements added to enhance the material resistance to corrosion. This material is commonly used for parts in contact with ionic solutions, known to induce surface pitting and corrosion, including sodium chloride [17]. The impact of the pore structure, porosity and carbon source flow distribution across the SS materials on the graphene homogeneity was also investigated by growing graphene on non-woven flat sheets. Growth

conditions, including growth time, carbon source flow rate and growth temperature were investigated. It was shown that the graphene coatings could be finely grown on the SS surface from a few layers thick to complex interconnected macro-flakes. The presence of the continuous graphene meso-structure around the stainless steel fibres that form the substrate enhances the resistance of the metal membrane materials to corrosion in synthetic seawater, while sharply increasing their electrical conductivity and specific surface area.

2. Materials and methods

The porous stainless steel non-woven flat sheet samples Bekipor SS316 were sourced from Bekaert Fibre Technology (Marietta – GA, USA) and provided by BOSFA Pty Ltd (Kewdale WA, Australia), part of the Bekaert group. These porous stainless steel substrates were made of sintered metal fibres with standard 316SS grade stainless steel of typical composition iron (Fe), <0.03% carbon (C), 16–18.5% chromium (Cr), 10–14% nickel (Ni), 2–3% molybdenum (Mo), <2% manganese (Mn), <1% silicon (Si), <0.045% phosphorus (P) and <0.03% sulphur (S). The diameter of the stainless steel fibres measured by Scanning Electron Microscopy (SEM) was found to be $15 \pm 0.5 \mu\text{m}$. The samples were cut, manually cleaned with ethanol and dried with compressed air prior to graphene growth.

Graphene growth was performed in a low-vacuum chemical vapour deposition set-up using a tube furnace from Lenton, model LTF 14/50/450. After loading the samples into a ceramic boat, the tube was pumped down for 30 min at 10 Pa. Then a mixture of Ar/H₂ (85/15 – >99.9%) was used to flush the tube and samples, for 15 min at 533 Pa and a flow rate of 400 cubic centimetre per minute (ccm), to remove any remaining oxygen prior to the growth. After a 5 min extra degassing in high vacuum, a series of samples were prepared by adjusting the growth time (0–60 min), temperature (800–1000 °C) and hexane flow rate (0–30 ccm) using analytical grade hexane (purity >99.9% Sigma Aldrich). The hexane pressure within the tube furnace during graphene growth was maintained constant at 533 Pa. The samples were cooled at 5 °C/min to <100 °C prior to being removed from the furnace and stored in a dry place. Gas pressures, temperatures and flow rates were recorded and showed relative variations lower than 1%.

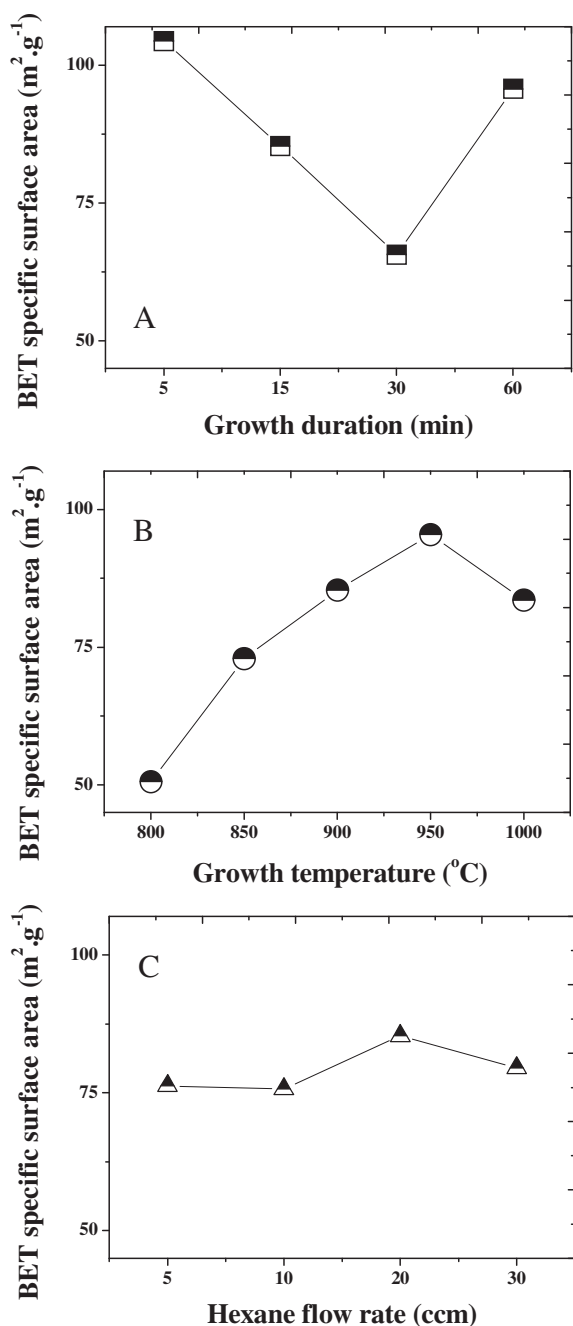


Fig. 3 – BET surface area for (A) the growth duration, (B) the growth temperature and (C) the hexane flow rate series.

The samples were characterised by Scanning Electron Microscopy (SEM) on a Quanta dual beam SEM (5 keV, 10 mm working distance). Energy Dispersive Spectroscopy (EDS) was performed with an EDAX system on the SEM (20 keV, 10 mm working distance). Ion beam milling was performed with the Gallium (Ga) Focus Ion Beam (FIB) on the Quanta. The first cuts were performed at a voltage of 20 keV and intensity of 15 nA. Cleaning was performed at 20 keV and two consecutive steps at 1 nA and 0.33 nA. Image analysis was performed with GIMP 2.8. For XPS, the instrument used was an AXIS Nova (Kratos Analytical Ltd, UK). The samples were irradiated with Al K α radiation ($h\nu = 1486.6$ eV) from

a mono-chromated source operating at 150 W. Survey spectra were acquired at a pass energy of 160 eV, and 1 eV/step. Region spectra were acquired at a pass energy of 20 eV, and 0.1 eV/step. The particulates were immobilised by pressing into double-sided carbon tape. The pressure in the analysis chamber was 5E – 9 torr, or lower. Low-energy electrons were directed at the sample surfaces during irradiation to compensate for surface charging. Raman spectroscopy was performed on a Renishaw apparatus with a 514 nm excitation laser wavelength at room temperature. The D/G ratios were calculated by the intensity ratio between the peaks at around 1360 cm⁻¹ (D peak) and 1560 cm⁻¹ (G peak). Contact angle measurements were performed on a goniometer. The size of the droplet used for contact angle was 4 μ L and the image was systematically taken 3 s after placing the droplet on the surface and an average of 3 different measurements is reported. The specific surface area of the samples was determined by Brunauer–Emmett–Teller (BET) surface analysis across a pressure range of $p/p_0 = 0.1$ – 0.3 at 77 K on a Micromeritics Tristar 3000. Samples were degassed for at least 12 h in pure nitrogen at 100 °C prior to performing the adsorption. Corrosion tests were performed using a previously described procedure and system [18]. Electrochemical tests were performed using a three electrode flat-cell which consisted of an immersed working electrode area of ~ 0.07 cm², a saturated calomel (SCE) reference electrode and a carbon counter electrode. The samples were cut into 1 cm² squares, welded to a copper wire, embedded into an insulating epoxy resin (RESINE MA2+ from PRESI SA, France) and cured for 6 h. All tests were carried out in 3.5 wt% NaCl and the polarisation tests were started after 5 min of immersion to allow for wetting of the surface. Anodic and cathodic scans were performed independently due to the potentially fragile nature of the graphene layer [19]. Data analysis and peak fitting for the different tests were performed with Origin Pro 8.0.

3. Results and discussion

The non-woven materials used in this study were composed of 15 μ m diameter SS316 fibres. An average pore size distribution of these materials was previously estimated to be ~ 20 μ m with a porosity of $\sim 45\%$ [20]. The formation of porous graphene coatings by CVD on the surface of the porous SS316 fibres composing the non-woven is demonstrated in Figs. 1 and S1. The deposition mechanisms leading to the formation of a controlled thickness of graphene, ranging from few layers to micron sized graphite, were found to largely depend on the growth conditions, including the CVD duration, plateau temperature and carbon source flow rate in the furnace.

In the first part of these experiments the impact of the growth duration at a fixed carbon source flow rate and CVD temperature was studied (Fig. 2). As seen in Fig. 2 (left), for very short growth times, and typically below 2 min, ultra-thin and discrete graphene sheets are formed on the metal substrate. These initial sheets are observed to grow as a function of time prior to forming a rough but continuous coating on the surface of the metal fibres between 2 and 5 min of growth time (Fig. 2 right). Based on BET surface area calculations, the

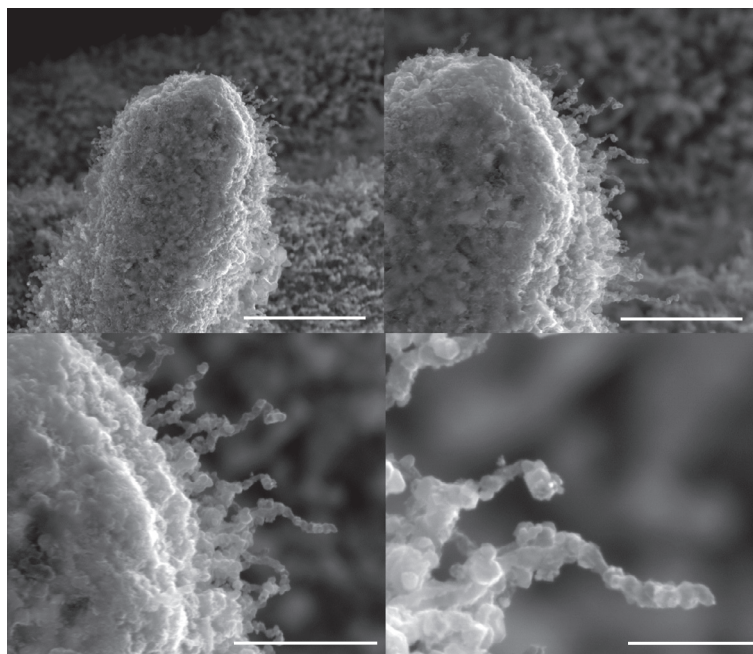


Fig. 4 – Nano-pillars structure at 30 ccm hexane flow feed, 900 °C and for 15 min of growth. The scale bars respectively correspond to (top left) 10, (top right) 5, (bottom left) 1 and (bottom right) 0.5 μm.

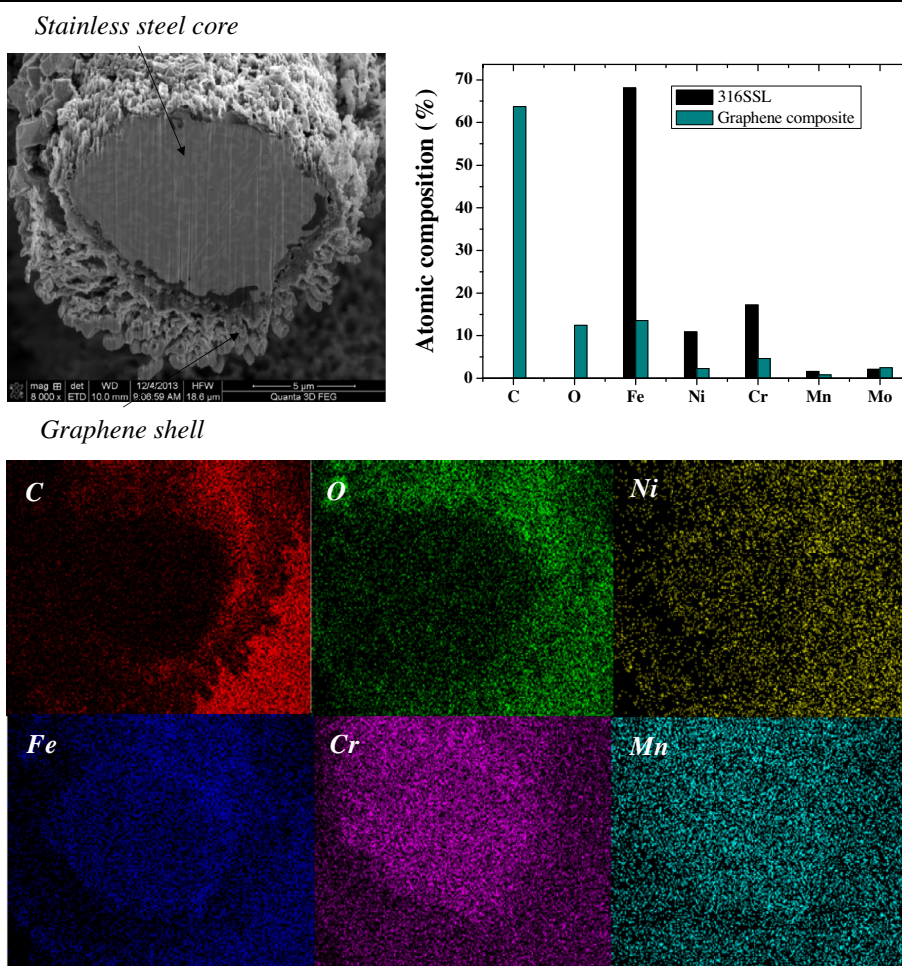


Fig. 5 – EDS mapping and SEM of a FIB milled cross section of a 900 °C, 15 min, 20 ccm hybrid stainless steel graphene sample. The scale bar on the SEM is 5 μm and all elemental maps are equally scaled up in intensity and contrast. Surface mappings are available in Fig. S3. (A colour version of this figure can be viewed online.)

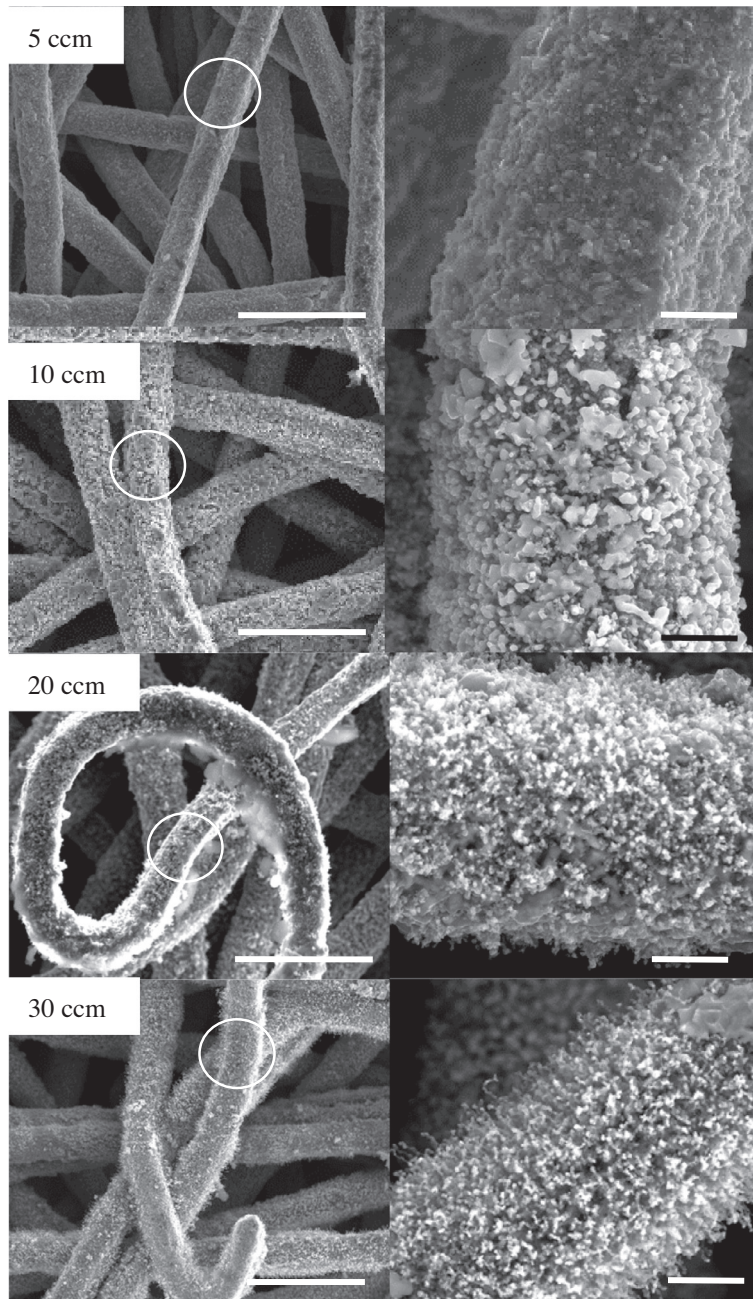


Fig. 6 – Representative SEMs of the hybrid stainless steel graphene samples for a series of carbon source flow rates (at 900 °C and 15 min growth time). The areas highlighted on the left column of images with white circles correspond to the higher magnification on the right hand side column. Scale bars for the left and right image columns are 50 μm and 5 μm , respectively.

presence of the nano-pillars massively increased the specific surface area of the bare stainless steel material by more than 26,000 times from 0.004 to approximately 105 m^2/g (Fig. 3). Interestingly, no clear change of specific surface area was found as a function of the hexane flow rate while the increasing growth temperature between 800 and 950 °C led to an increase of the surface area by more 95%. In addition, the growth duration was found to play a role with lower growth duration typically leading to the highest specific surface area, as suggested by the SEMs in Fig. 2. Past this time and up to

15 min, the graphene deposition started to be anisotropic resulting in highly regular and homogeneous nano-pillar outgrowth from the surface of the metal to form a highly porous and hairy shell around the metal fibres (Fig. 1). The length of these graphene nano-pillars was found to be between 1 and 2 μm . For longer growth times, and thus larger amounts of graphene deposition, the nano-pillars were shown to coalesce forming semi-dense shells with a thickness between 2 and 5 μm (Fig. 4). Cross-sections of the shells and nano-pillar coatings were obtained by FIB milling to reveal the formation of a

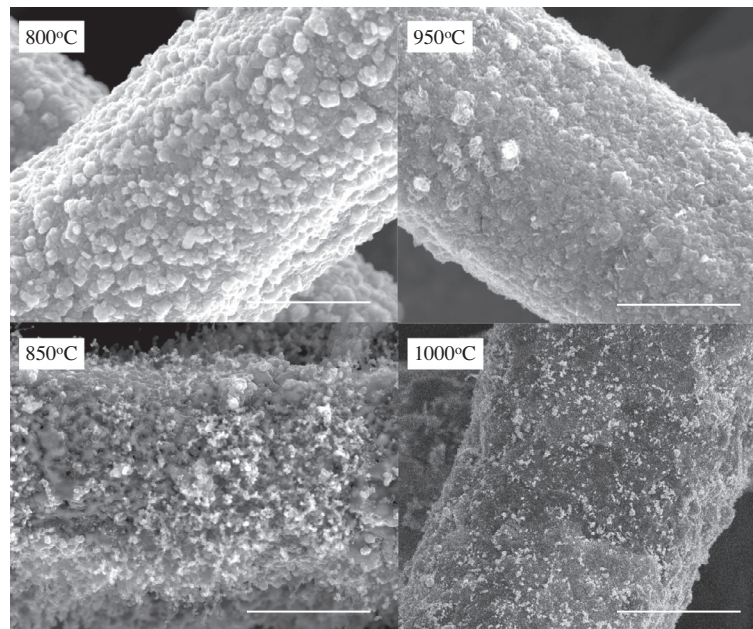


Fig. 7 – Impact of the growth temperature for 15 min growth times at 20 ccm hexane flow rate on the formation of the graphene shells. Images for the 900 °C are given in the main body of the manuscript. Scale bars are all corresponding to 5 μm .

highly ordered and nearly pure carbon composed nano-material (Fig. 5).

Furthermore, the flow rate of the carbon source plays a fundamental role in the formation of the nano-pillars. As seen in Fig. 6, when the hexane flow rate was changed between 5 and 30 ccm, the density at 900 °C and for 15 min of growth time was found to gradually increase with the carbon source flow rate. Dis-continuous deposition was found to occur below a 20 ccm flow rate suggesting that a minimum concentration of carbon source is required to form the sheets on the metal fibres. In general, graphene materials of a few layers thick may be formed when the amount of carbon dissolved in the metal is low [21]. This is the reason why graphene monolayers can statistically be more likely formed with Ni than Cu metal substrates and high crystallinity graphene formed at very low carbon source flow rates [22,23]. The presence of grains on the surface of the metal fibres rich in metals with higher solubility of carbon should lead more realistically to the formation of nano-pillars. The distribution of Cr and Ni across the surface of the SS316 material may also play a role in the homogeneity of the coating and in the growth of the graphene sheets. Indeed these metals are known to lead to the catalytic growth of graphene and could thus seed graphene growth across the surface of alloys as previously reported [21]. Cr may indeed be more present on the surface of the fibres due to precipitation upon cooling during metal casting. The cooling rate after graphene deposition may also play a role due to the difference in expansion coefficient between graphene and the SS316 substrate which could lead to temperature variations and thus thermal stress gradients across the hybrid graphene/metal fibres [24]. These results reinforce the hypothesis previously discussed that the size and the microstructure of the grains may play a role in the graphene growth conditions, as previously extensively discussed for copper and other pure metals substrates [25–27].

The highly inhomogeneous nature of stainless steel, both in terms of grain size distribution and microstructure would likely hinder the formation of highly crystalline and high grade graphene [21]. The crystalline structure of austenitic stainless steels is face cubic centred while that of copper is cubic close packed, and therefore offer a better match with the hexagonal structure of graphene [21,26]. As previously shown, the size and the microstructure of the metal surface grains will be critical to the formation of high crystallinity graphene and the initial carbon deposition for the first layer is thought to match the surface lattices of the metal grains [28]. The growth of stable and high grade graphene on the surface of SS is therefore more challenging due to the combined rough nature of the metal fibres and to a stronger mismatch with the honeycomb-type, non-Bravais, lattice of graphene and that of the heterogeneous SS microstructure [29].

The growth of graphene from SS surfaces is likely catalysed by the presence of Ni or Cr present across the surface of the metal grains as previously demonstrated [30]. The curvature of the fibres may also enhance the formation of homogeneous graphene sheets. Indeed, as seen in Fig. S1 and visible in Fig. 2 by transparency, the size of the metal grains across the pristine SS316 fibres before any treatment is on the order of 3–5 μm suggesting that each fibre might be composed of up to 3–4 grains in section. These non-optimal substrate conditions, compared to previously reported growth of graphene on metal alloys such as stainless steel, further reinforce the potential of the technique for the decoration and protection of porous metal materials. Furthermore, this phenomenon may be closely related to the carburization of steel which is a metallurgical hardening process whereby iron or steel materials absorb carbon liberated when a decomposing carbon source, such as charcoal or carbon monoxide, is put in contact with the hot metal surface. The degree of carburization will depend largely on the duration and operation tem-

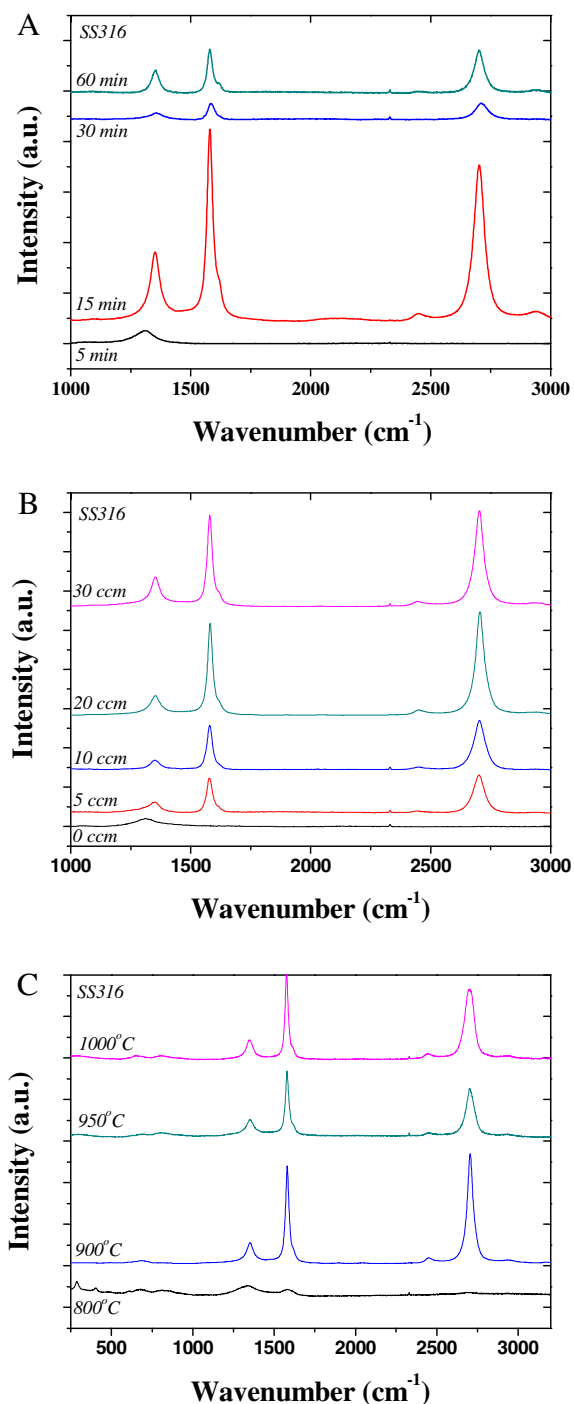


Fig. 8 – Raman spectra for the time base (A), hexane flow rate base (B) and temperature base (C). The baseline of the curves were offset by a constant distance (8% of total scale) for clarity. (A colour version of this figure can be viewed online.)

perature of the process and carbon diffusion across the matrix may vary across the thickness of the material. Longer carburizing durations and higher temperatures were shown to typically increase the depth of carbon diffusion while rapid quenching may generate a larger carbon gradient with a richer metal surface and a leaner metal core. The higher carbon content on the outer surface may therefore cause crys-

talline structure shifts from tetragonal to body centred tetragonal, locally changing the austenitic metal to a martensitic one and deforming the shape of the grains [31]. The similarity of the carburization process and the conditions of the CVD growth of graphene may therefore lead to such changes and explain the distribution of the nano-pillars and graphene shells due to a gradient of catalytic metals, necessary for graphene growth and to a stronger distribution of carbons upon degradation of the carbon source.

In addition, the CVD growth temperature was also found to have a strong impact on the structure and kinetics of formation of the graphene nano-pillars and shells. As seen in Figs. 6 and 7, the size and density of the nano-pillars for 15 min of growth time and 20 ccm of hexane flow rate were found to progressively increase with CVD temperature up to 850–900 °C. Although the nano-pillar density was already relatively high at 850 °C, and a number of patches were clearly visible on the surface of the fibres, the maximum coverage density of nano-pillars was found at 900 °C (Fig. 1). Interestingly, only a limited number of nano-pillars are visible at 950 °C while none are left at 1000 °C (Fig. 7) suggesting that the amount of free carbons is higher at temperatures above 900 °C leading to more distributed deposition across the surface. The formation of the nano-pillars may therefore be rendered unstable past this point to the addition of large amount of amorphous carbons leading to the formation of the porous shells shown in the cross section SEMs in Fig. 5. An interesting analogy lies with the growth of carbon nanotubes (CNTs) since catalytic iron oxide nano-particles are used for their growth by CVD. However, the discrete and homogeneous distribution of iron oxide nano-particles during CVD of CNTs, allows for the formation of highly crystalline and long range ordered carbon nanostructures, very different from those here reported. It is however possible that, due to localised oxidation of the stainless steel and thus of the containing iron metal, multi-walled CNTs may have been wrapped with amorphous carbon as the constituents of the nano-pillars. This special formation may alter the nature of the passivation process and the increase in the electrical conductivity at the interface between the metal and the liquid solution. This optimum growth temperature might here be related to the activation of the metal substrate as previously reported [25,32]. In addition, the presence of oxygen in the shell, and at the interface between the metal and the graphene, clearly visible on the EDS mappings in Fig. 5, is likely due to the formation of iron oxides upon annealing of the structure. Minute amounts of Fe, Ni and Cr were also found to have migrated and doped the carbon shells. This is assumed to be related to the diffusion of metals upon annealing at high temperature in the presence of H₂. Although critical to the growth of graphene to stitch aromatics rings upon deposition on the metal grains [27,33], H₂ may also lead to the damage of the metal microstructure by forming metal hydrides [34]. As seen in Fig. S1, where the impact of the annealing temperature on the bare metal alone was studied free of carbon source, the microstructure of the metal is shown to be strongly affected by the thermal treatment in the reductive environment. Although the texture of the metal fibres is found to be relatively constant up to 900 °C, larger grains were progressively formed and cracks appeared at 1000 °C. This result is

Table 1 – Raman D/G ratios for the growth time, hexane flow rate and growth temperature series.

Growth time (min) @20 ccm, 900 °C	I(D)/I(G)	Hexane flow rate (ccm) @15 min, 900 °C	I(D)/I(G)	Growth temperature (°C) @15 min, 20 ccm	I(D)/I(G)
5	1.88	5	0.50	800	1.21
15	0.38	10	0.65	850	1.02
30	0.97	20	0.64	950	0.76
60	0.44	30	0.83	1000	0.79

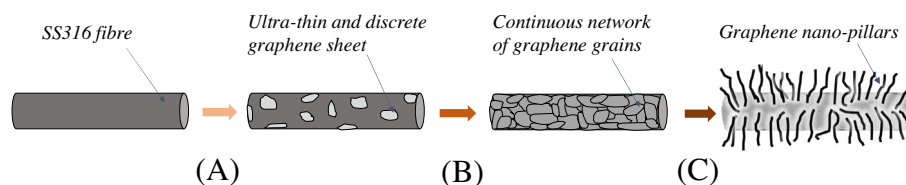


Fig. 9 – Schematic representation of the graphene growth steps with (A) the seeding of the surface with ultra-thin graphene layers, prior to (B) the formation of a continuous network made of graphene grains based on the microstructure of the underlining SS316 metal matrix and (C) the final growth of graphene nano-pillars and shells for extended growth times and carbon source feed flow rate. (A colour version of this figure can be viewed online.)

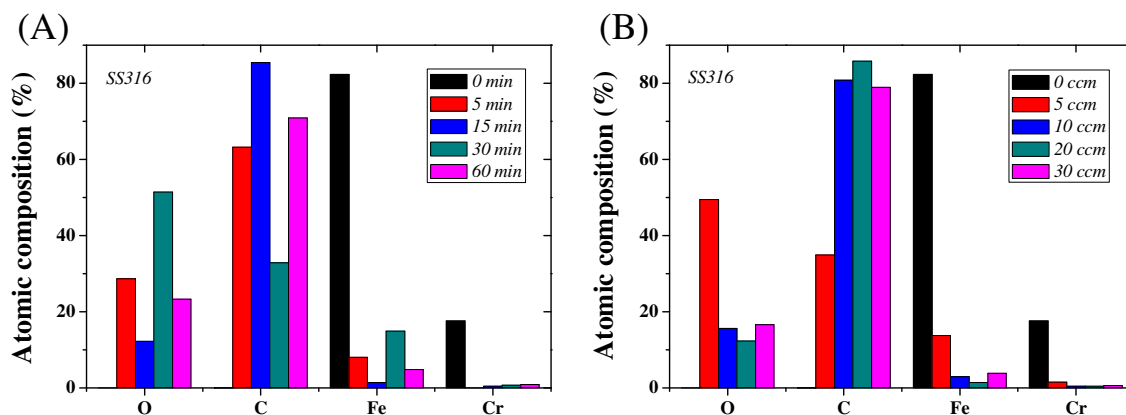


Fig. 10 – Atomic composition of the surface of the samples evaluated by XPS analysis for (A) the time series and (B) the hexane flow rate series. (A colour version of this figure can be viewed online.)

in agreement with previously reported ageing of SS316 at high temperature and for long exposure durations due to hydrogen embrittlement [35–37]. The formation of larger grains ultimately led to the formation of cracks across the metal fibres further suggesting accelerated ageing of the thin metal fibres at high temperature (Fig. S2).

However, due to the absence of oxygen gas in the growth process, the presence of oxygen-rich groups on the graphene material is, however, likely due to post-growth oxidation of the samples with air or moisture. This might indicate that upon formation surface vacancies are present on the graphene nano-wires making them prone to further reaction. The grade of the graphene and the presence of surface defects across the crystalline planes were therefore investigated by Raman spectroscopy which was used to characterise the vibrational modes of surface functional groups, and give indi-

cations of change across the graphitic carbon lattice [38,39]. The three peaks visible at 1355, 1599 and 2687 cm^{-1} on the Raman spectra in Fig. 8 are assigned to the D, G and 2D bands of the graphitic walls, respectively (Table 1). The D peak is an indicator of disorder in the carbon lattice and of amorphous carbon sites, while the G peak represents ordered sp^2 carbon domains [40]. The empirical Tuinstra–Koenig relation [41] which is the ratio of the intensity of the D and G peaks, provides an indication of the degree of order across graphitic plans. The intensity ratio of the 2D-band to the G-band on the Raman spectra was used to evaluate the number of layers across the graphene coatings with smaller ratios indicating the presence of larger numbers of layers [42,43]. The analysis of this ratio for the CVD grown graphene spectra presented in Fig. 7 demonstrate that multi-layer graphene sheets are formed for increasing CVD synthesis durations. The presence

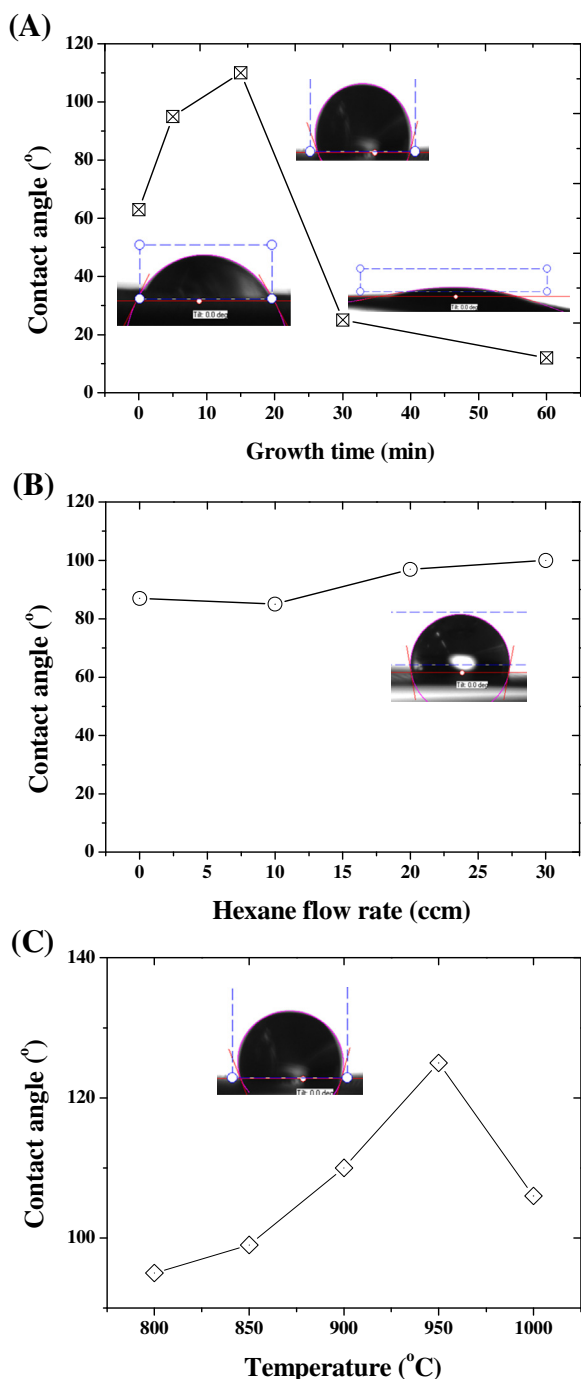


Fig. 11 – Water contact angle on (A) the growth time series (900 °C and 200 ccm hexane flow rate), (B) the hexane flow rate series (900 °C and 15 min growth time) and (C) the temperature series (20 ccm hexane flow rate and 15 min growth time). (A colour version of this figure can be viewed online.)

of defects across the crystalline graphitic plans was also assessed by analysing the I_D/I_G ratio. The ratio was shown an increase trend as a function of synthesis duration suggesting the presence of larger densities of defects for longer CVD growth durations except 5 min (Fig. 8A and Table 1). As seen in Fig. 8B where the impact of the carbon source flow rate

on the growth were investigated, although increasing carbon source flow rates are shown to lead to thicker structures, with up to 5 layers, the crystallinity of the graphitic plans is satisfactory given the non-optimal surface of the metal fibres and very few defects can be detected. At a hexane flow rate of 20 ccm, a full width at half maximum (FWHM) of 44.97 cm^{-1} was measured indicative of a single Lorentzian shaped peak at 2705 cm^{-1} for the 2D band, with a G to 2D intensity ratio $I_{2D}/I_G \approx 1.89$ corresponding to 2–3 layers of graphitic planes. Furthermore, as seen in Fig. 8C, an optimum of graphene quality was achieved at 850 °C. This result is again suggesting the formation of only up to 2 layers of high grade graphene at lower growth temperatures. Interestingly, the lowest quality graphene was achieved for the samples grown at 900 °C and for 15 min at 20 ccm hexane flow rate, corresponding to the optimum formation point of nano-pillars. This is suggesting that the nano-pillars, as expected from the SEMs, are not purely graphene and are probably composed of mixed amorphous and crystalline carbon materials. The Raman signal is however composed of both that of the coating and of the nano-pillars. The quality of the graphene below the nano-pillars is therefore likely comparable to that of the other temperatures at 850 and 950 °C.

The growth of the graphene nano-pillars across the surface of the SS316 fibres therefore appears to be kinetically related to the amount of carbon source injected in the furnace. A schematic of the growth mechanism is depicted in Fig. 9 highlighting the 3 distinct phases in the graphene coating formation as a function of the growth duration. In the first step of the mechanism, decomposed carbon feed material is deposited on the surface of the metal grains forming a discontinuous network of sheets made of a few layers of graphene. Then for larger flow rates or growth duration, a percolation threshold is reached leading to the formation of a semi-dense coating on the surface of the metal. Beyond this point, nano-pillars will grow from imperfections across the metal crystalline lattices, ultimately leading to the formation of dense and thick graphene shells for longer times. Furthermore, the density of the nano-wires on the SS fibre surface was found to be sharply increased between 10 and 30 ccm suggesting a direct impact of the degree of oxidation of the carbon source in contact with H_2 on the nucleation density of nano-pillars on the metal substrate [27,33].

In addition to the morphology of the coating, the grade of the graphene was also investigated. As seen across the Raman spectra presented in Fig. 8 and Table 1, although the highest grade graphene was achieved at 900 °C, reinforcing previously speculated arguments, the lowest D/G peak ratios were obtained between 10 and 20 ccm of hexane flow rate. This suggests that above 20 ccm, the amount of carbon available, despite leading to an increase of the nano-pillar density, leads to the deposition of a larger amount of amorphous carbon, potentially unreacted, on the surface of the fibres. This was also confirmed by the EDS mappings shown in Fig. S3, where the amount of oxygen was found to be much higher on the surface of the metal fibres at 30 ccm as opposed to 20 ccm. Interestingly, the highest D/G ratios for the growth duration series were found for the shortest time of 5 min, suggesting that the initial graphene sheets formed are of higher grade than the thicker coatings later generated (Table 1). Furthermore, as seen

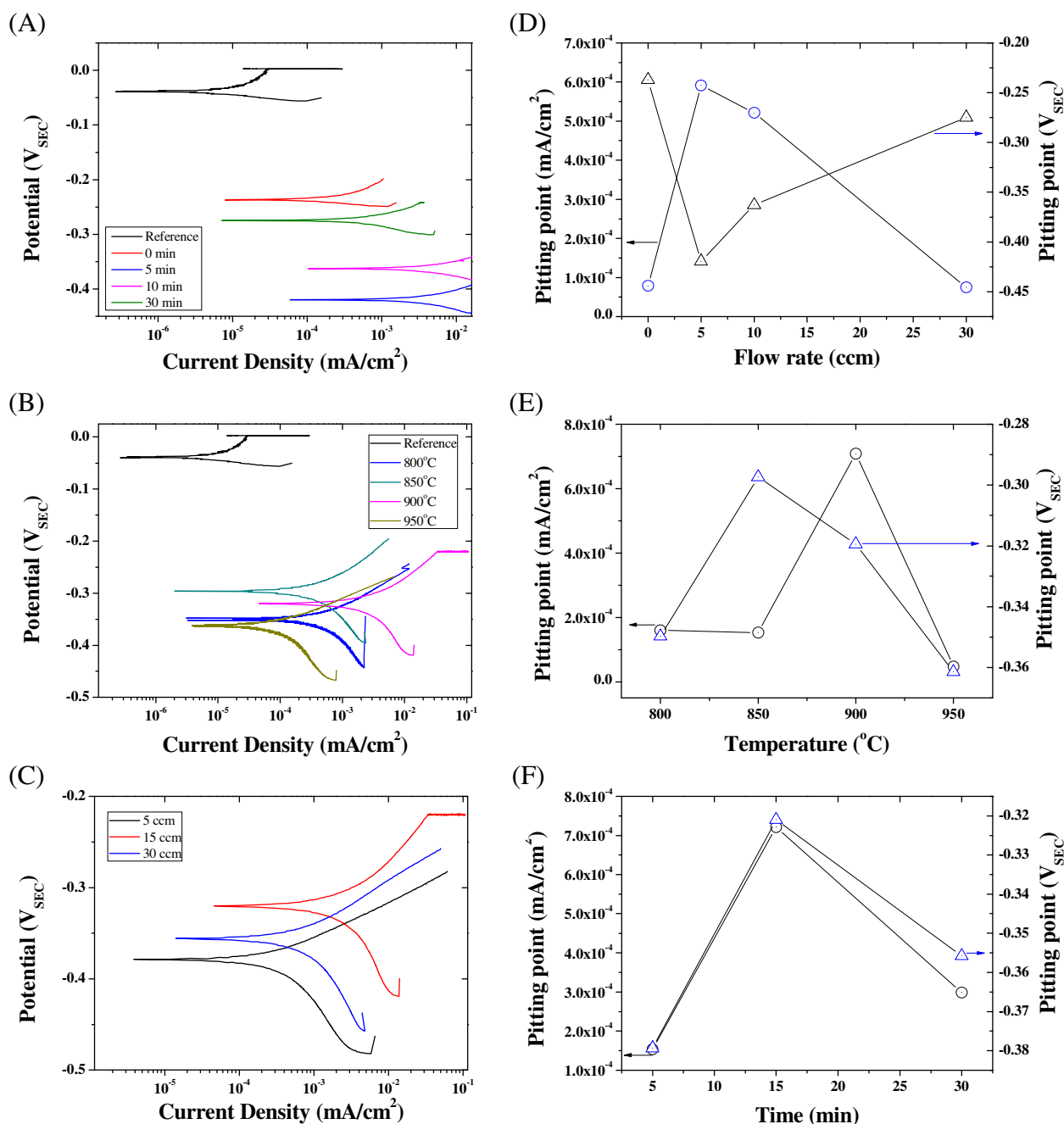


Fig. 12 – Corrosion tests for the SS316 in NaCl (3.5 wt% concentration) as a function of (A) time of hexane flow duration at 900 °C and 10 ccm of hexane flow rate, (B) CVD temperature for 10 min hexane flow rate and 15 ccm flow rate and (C) hexane flow rate at 900 °C and 15 min. Pitting points evaluated from the corrosion curves presented in (A), (B) and (C), for (D) the flow rate, (E) the time and (F) the temperature series on the SS316 samples. (A colour version of this figure can be viewed online.)

in Fig. 10, the carbon content was maximum at 15 min of growth duration and was relatively constant past 5 ccm of hexane flow rate confirming the formation of a network of graphene above 10 ccm. Shorter times and lower carbon source flow rates are therefore shown to lead to the deposition of more amorphous carbon materials.

The wettability of the structures, which is directly related to the crystallinity and to the presence of functional groups

on the graphene surface was also studied by performing contact angle measurements on the samples. As seen in Fig. 11, the hydrophobicity of the samples progressively increases up to 15 min of growth prior to sharply decreasing for longer growth durations. This result strongly supports the Raman and XPS data demonstrating the presence of amorphous carbons for long growth durations. In addition, no statistical variations were visible across the series of hexane flow rates

while the maximum contact angle was found between 900 and 950 °C of growth temperature also supporting the data showing that the highest nano-pillar densities were achieved at temperatures around 900 °C thus highlighting the hydrophobic nature of the nano-pillars. Interestingly, the ageing of the native stainless steel fibres was also visible on the XPS data. The heat treatment which the metal underwent lead to leaching of Molybdenum (Mo), part of the stainless steel alloy, potentially in the form of precipitates, which lead to an increase of the surface content of Mo across the fibres and hybrid composites.

Corrosion resistance was investigated by measuring the pitting potential for the series of samples. Graphene was previously shown to act as a corrosion inhibitor by simultaneously increasing the material surface conductivity and acting as a molecular barrier against the diffusion of corrosive agents towards sensitive surfaces [1,19]. As seen in Fig. 12A–C, the corrosion resistance of the metal was strongly improved with the highest current densities obtained at 900 °C and for shorter periods of growth durations. The polarisation curves for the graphene coated SS316 samples present a sharp decrease in both the anodic and cathodic reaction rates (Fig. 12), suggesting that the graphene layer is providing protection to the underlying surface by slowing down the ionic transfer from the bulk solution and their reaction with the metal surface. The graphene coated metal fibres offer a decrease in absolute corrosion current density, and the corrosion potential, typically referred to as the pitting point, is shown to shift by nearly 50% while also increasing the current density by up to 6 times. Interestingly, the enhanced electro-chemical properties are closely related to the presence of the nano-pillars and to the specific surface area of the materials, since the highest corrosion resistance are reported for the samples grown across the range 850–900 °C and for the lowest carbon source flow rates. Although the impact of the CVD growth duration was more modest, the best samples were yet obtained after 15 min of growth, which is highly consistent with the morphological and surface characterisation data previously shown. The pitting current density and potential values for the series of samples are shown in Fig. 11D–F. The shift of pitting point is suggesting that the graphene is acting primarily as an anodic barrier to ion diffusion towards the underlying metal surface thus decreasing the corrosion rate by reducing the kinetics of metallic ionisation [19,44]. Interestingly, no impact of the specific surface area of the hybrid materials, which should enhance the corrosion kinetics, was found here, suggesting the presence of the near-defect free graphene coating or shells across the surface of the metal fibres. The incorporation of graphene may therefore shift the potentional dynamic plots to more positive potentials, suggesting a more noble behaviour for the systems. This might be related to the presence of the high density nano-pillars for these series of samples which could act as a passivation promoter simultaneously protecting and increasing the conductivity of the interface between the metal and the liquid solution. Although the precise nature of the passivation process is not clearly determined here, Schottky barriers are often used to evaluate metal – graphene interfacial junctions [10,13]. The hybridization of graphene with metal

surfaces may open a band gap in the semi-metallic graphene, resulting in semiconducting behaviour for the metal-graphene interface [19,45]. These interfaces were recently shown to lead to facilitated electron transfer which, in turn, reduces the kinetics of the corrosion reactions by restricting the flow of electrons to the metal surface [45]. The impact of the graphene coating thickness is also clearly visible for the hexane flow rate series since the highest pitting current density was obtained for 30 ccm, the larger hexane flow rate. As expected, this is suggesting that the thicker coating leads to better corrosion inhibition. The potential of graphene coatings formed by CVD across complex and rough metal surfaces was therefore demonstrated and the presence of the nano-pillars shown to likely enhance the corrosion resistance and electron transport properties of the materials.

4. Conclusions

The growth of porous graphene sheets and graphene nano-flakes was demonstrated for the first time across porous metallic structures. Through highly controlled growth conditions, 3D networks of graphene can be generated completely covering the base metal surface. Furthermore, the presence of the graphene was shown to highly enhance corrosion resistance and electrical conductivity of the materials without otherwise altering the properties of the stainless steel. This new approach is opening the route to the facile fabrication of advanced surface coatings with potential applications in developing novel thermal exchangers, separation, specific adsorption and bio-compatible materials.

Acknowledgements

The authors acknowledge the Cooperative Research Network (CRN2012/2) initiative of the Australian Department of Industry and Dr. DUMEE's Alfred Deakin Fellowship for funding and supporting this work. They also thank Dr. Mark Nave and Dr. Andrew Sullivan for fruitful discussion for SEM imaging, Dr. Pimm Vongsvivut for assistance with Raman spectroscopy (Waurm Ponds, Victoria – Australia) and Dr. Rob Jones (Latrobe University, Victoria – Australia) for assistance with XPS data analysis.

Appendix A. Supplementary data

Supplementary data associated with this article can be found, in the online version, at <http://dx.doi.org/10.1016/j.carbon.2015.02.042>.

REFERENCES

- [1] Singh Raman RK, Chakraborty Banerjee P, Lobo DE, Gullapalli H, Sumandasa M, Kumar A, et al. Protecting copper from electrochemical degradation by graphene coating. *Carbon* 2012;50(11):4040–5.
- [2] Dumeé LF, He L, Lin B, Ailloux F-M, Lemoine J-B, Velleman L, et al. The fabrication and surface functionalization of porous

- metal frameworks – a review. *J Mater Chem A* 2013;1(48):15185–206.
- [3] Saji VS. A review on recent patents in corrosion inhibitors. *Recent Pat Corros Sci* 2010;2:6–12.
- [4] Sim S, Cole IS, Choi YS, Birbilis N. A review of the protection strategies against internal corrosion for the safe transport of supercritical CO₂ via steel pipelines for CCS purposes. *Int J Greenhouse Gas Control* 2014;29:185–99.
- [5] Little B, Lee J, Ray R. A review of ‘green’ strategies to prevent or mitigate microbiologically influenced corrosion. *Biofouling* 2007;23(1–2):87–97.
- [6] Zheludkevich M. Self-healing anticorrosion coatings. Self-healing materials. Wiley-VCH Verlag GmbH & Co. KGaA; 2009. p. 101–39.
- [7] Tatsuma T, Saitoh S, Ohko Y, Fujishima A. TiO₂–WO₃ photoelectrochemical anticorrosion system with an energy storage ability. *Chem Mater* 2001;13(9):2838–42.
- [8] Wang H, Akid R. A room temperature cured sol–gel anticorrosion pre-treatment for Al 2024–T3 alloys. *Corros Sci* 2007;49(12):4491–503.
- [9] Novoselov KS, Fal’ko VI, Colombo L, Gellert PR, Schwab MG, Kim K. A roadmap for graphene. *Nature* 2012;490(7419):192–200.
- [10] Gaikwad AV, Rout TK, Van der Plas D, Dennis RV, Banerjee S, Pacheco Benito S, et al. Carbon nanotube/carbon nanofiber growth from industrial by-product gases on low- and high-alloy steels. *Carbon* 2012;50(12):4722–31.
- [11] Mayavan S, Siva T, Sathiyarayanan S. Graphene ink as a corrosion inhibiting blanket for iron in an aggressive chloride environment. *RSC Adv* 2013;3(47):24868–71.
- [12] Prasai D, Tuberquia JC, Harl RR, Jennings GK, Rogers BR, Bolotin KI. Correction to graphene: corrosion-inhibiting coating. *ACS Nano* 2012;6(5):4540.
- [13] Dennis RV, Viyanalage LT, Gaikwad AV, Rout TK, Banerjee S. Graphene nanocomposite coatings for protecting lowalloy steels from corrosion. *Am Ceram Soc Bull* 2013;92(5):18–24.
- [14] Dumée LF, Feng C, He L, Yi Z, She F, Peng Z, et al. Single step preparation of meso-porous and reduced graphene oxide by gamma-ray irradiation in gaseous phase. *Carbon* 2014;70:313–8.
- [15] Jiang L, Fan Z. Design of advanced porous graphene materials: from graphene nanomesh to 3D architectures. *Nanoscale* 2014;6(4):1922–45.
- [16] Han S, Wu D, Li S, Zhang F, Feng X. Porous graphene materials for advanced electrochemical energy storage and conversion devices. *Adv Mater* 2014;26(6):849–64.
- [17] Tan Y, Liu T. Characterising localised corrosion inhibition by means of parameters measured by an electrochemically integrated multielectrode array. *Corros Eng Sci Technol* 2014;49(1):23–31.
- [18] Xiong J, Tan MY, Forsyth M. The corrosion behaviors of stainless steel weldments in sodium chloride solution observed using a novel electrochemical measurement approach. *Desalination* 2013;327:39–45.
- [19] Kirkland NT, Schiller T, Medhekar N, Birbilis N. Exploring graphene as a corrosion protection barrier. *Corros Sci* 2012;56:1–4.
- [20] Dumée LF, Allieux F-M, Reis R, Duke M, Gray S, Tobin M, et al. Qualitative spectroscopic characterization of the matrix–silane coupling agent interface across metal fibre reinforced ion exchange resin composite membranes. *Vib Spectrosc* 2014.
- [21] Robin J, Ashokreddy A, Vijayan C, Pradeep T. Single- and few-layer graphene growth on stainless steel substrates by direct thermal chemical vapor deposition. *Nanotechnology* 2011;22(16):165701.
- [22] Koos AA, Murdock AT, Nemes-Incze P, Nicholls RJ, Pollard AJ, Spencer SJ, et al. Effects of temperature and ammonia flow rate on the chemical vapour deposition growth of nitrogen-doped graphene. *Phys Chem Chem Phys* 2014;16(36):19446–52.
- [23] Umair A, Raza H. Controlled synthesis of bilayer graphene on nickel. *Nanoscale Res Lett* 2012;7(1):437.
- [24] Reina A, Thiele S, Jia X, Bhaviripudi S, Dresselhaus M, Schaefer J, et al. Growth of large-area single- and Bi-layer graphene by controlled carbon precipitation on polycrystalline Ni surfaces. *Nano Res* 2009;2(6):509–16.
- [25] Wang G, Zhang M, Zhu Y, Ding G, Jiang D, Guo Q, et al. Direct growth of graphene film on germanium substrate. *Sci Rep* 2013:3.
- [26] Miller DL, Keller MW, Shaw JM, Rice KP, Keller RR, Diederichsen KM. Giant secondary grain growth in Cu films on sapphire. *AIP Adv* 2013;3(8).
- [27] Losurdo M, Giangregorio MM, Capezzuto P, Bruno G. Graphene CVD growth on copper and nickel: role of hydrogen in kinetics and structure. *Phys Chem Chem Phys* 2011;13(46):20836–43.
- [28] Muñoz R, Gómez-Aleixandre C. Review of CVD synthesis of graphene. *Chem Vap Deposition* 2013;19(10–12):297–322.
- [29] Zhao L, Rim KT, Zhou H, He R, Heinz TF, Pinczuk A, et al. Influence of copper crystal surface on the CVD growth of large area monolayer graphene. *Solid State Commun* 2011;151(7):509–13.
- [30] Ning J, Hao L, Zhang X, Liang M, Zhi L. High-quality graphene grown directly on stainless steel meshes through CVD process for enhanced current collectors of supercapacitors. *Sci China Technol Sci* 2014;57(2):259–63.
- [31] Sudha C, Sivai Bharasi N, Anand R, Shaikh H, Dayal RK, Vijayalakshmi M. Carburization behavior of AISI 316LN austenitic stainless steel – experimental studies and modeling. *J Nucl Mater* 2010;402(2–3):186–95.
- [32] Faggio G, Capasso A, Messina G, Santangelo S, Dikonimos T, Gagliardi S, et al. High-temperature growth of graphene films on copper foils by ethanol chemical vapor deposition. *J Phys Chem C* 2013;117(41):21569–76.
- [33] Gan L, Luo Z. Turning off hydrogen to realize seeded growth of subcentimeter single-crystal graphene grains on copper. *ACS Nano* 2013;7(10):9480–8.
- [34] Sakintuna B, Lamari-Darkrim F, Hirscher M. Metal hydride materials for solid hydrogen storage: a review. *Int J Hydrogen Energy* 2007;32(9):1121–40.
- [35] Michler T, Naumann J. Coatings to reduce hydrogen environment embrittlement of 304 austenitic stainless steel. *Surf Coat Technol* 2009;203(13):1819–28.
- [36] Weber S, Martin M, Theisen W. Lean-alloyed austenitic stainless steel with high resistance against hydrogen environment embrittlement. *Mater Sci Eng A* 2011;528(25–26):7688–95.
- [37] Thomas RG, Yapp D. The effect of heat treatment on type 316 stainless steel weld metal welding research; 1978.
- [38] Ferrari AC, Basko DM. Raman spectroscopy as a versatile tool for studying the properties of graphene. *Nat Nanotechnol* 2013;8(4):235–46.
- [39] Vázquez-Santos MB, Geissler E, László K, Rouzaud J-N, Martínez-Alonso A, Tascón JMD. Comparative XRD, Raman, and TEM study on graphitization of PBO-derived carbon fibers. *J Phys Chem C* 2011;116(1):257–68.
- [40] Yang D, Velamakanni A, Bozoklu G, Park S, Stoller M, Piner RD, et al. Chemical analysis of graphene oxide films after heat and chemical treatments by X-ray photoelectron and micro-Raman spectroscopy. *Carbon* 2009;47(1):145–52.
- [41] Koenig FTaJL. Raman spectrum of graphite. *J Chem Phys* 1970;53(3):1126–30.

- [42] Ferrari AC, Meyer JC, Scardaci V, Casiraghi C, Lazzeri M, Mauri F, et al. Raman spectrum of graphene and graphene layers. *Phys Rev Lett* 2006;97(18):187401.
- [43] Hao Y, Wang Y, Wang L, Ni Z, Wang Z, Wang R, et al. Probing layer number and stacking order of few-layer graphene by Raman spectroscopy. *Small* 2010;6(2):195–200.
- [44] Rout TK, Jha G, Singh AK, Bandyopadhyay N, Mohanty ON. Development of conducting polyaniline coating: a novel approach to superior corrosion resistance. *Surf Coat Technol* 2003;167(1):16–24.
- [45] Songür M, Çelikkan H, Gökmeşe F, Şimşek SA, Altun NŞ, Aksu ML. Electrochemical corrosion properties of metal alloys used in orthopaedic implants. *J Appl Electrochem* 2009;39(8):1259–65.